Faculty and Researchers   Faculty and Researchers' Publications

Measurement of Large Angle Atomic Scattering Using Axially Symmetric Magnetic Fields

Bush, T.O.; Heinz, O.; Rodeback, G.W.; Cook, C.J.

American Institute of Physics

Measurement of Large Angle Atomic Scattering Using Axially Symmetric Magnetic Fields*

T. O. Bush,† O. Heinz, and G. W. Rodeback

Naval Postgraduate School, Monterey, California 93940

AND

C. J. Cook

Stanford Research Institute, Menlo Park, California 94025

(Received 23 May 1969)

A technique using the focusing properties of a nonuniform axially symmetric magnetic field to study large angle ($\theta > 32°$, lab) scattering of ions from atoms and molecules is described. The scattering cell is placed on the magnetic axis at the position of maximum field and ions in the momentum interval $|\Delta p|$ at $|p|$ scattered into a conical shell $\Delta\theta$ at θ are counted by a detector placed down along the axis in a region of low field. The solid angle is increased by a factor of several hundred over conventional scattering techniques of comparable angular resolution due to the azimuthal symmetry of the apparatus. The magnetic vector potential and the trajectory equation for a charged particle in this type of inhomogeneous, axially symmetric field are derived. As a preliminary test the known differential scattering cross section for He^+ on the He was measured from 40 to 52° (lab) at 300 eV. Results of measurements of the absolute differential scattering cross sections for Li^+ on He from 36 to 41.7° at 200 and 300 eV, corresponding to CM scattering angles of 90 to 160°, are presented.

INTRODUCTION

IN recent years the techniques for measuring differential scattering cross sections for various atomic and molecular processes have been improved to the point where very precise measurements can be made in almost routine manner. In the conventional approach a target of thickness t and gas density n particles/cm³ is confined in a cell within a surrounding vacuum. A well collimated beam of nearly monoenergetic ions of current I_i is projected into the target. A detector, subtending a solid angle

$$d\Omega(\theta) = \sin\theta d\theta d\phi \qquad (1)$$

at the interaction region, is placed at an angle θ to the incident beam and the number of particles/sec entering the detector, N_s, is measured. The scattered particles are usually detected as a current I_s where

$$I_s = N_s d\Omega(\theta). \qquad (2)$$

From these measured quantities, the differential scattering cross section in the laboratory coordinate system can be calculated as

$$d\sigma(\theta) = I_s / I_i n t d\Omega(\theta). \qquad (3)$$

However, in order to obtain reasonably good angular resolution, the solid angle normally includes only about 1° of the available 360° of azimuthal angle ϕ into which ions can scatter from the incident beam for a given value of θ. This restriction results in fairly small solid angles (about 10^{-4} sr) and sets a lower limit on observable differential scattering cross sections.

By modifying the techniques of thin lens β-ray spectroscopy, we have constructed an experimental apparatus,[1] shown schematically in Fig. 1, which collects essentially all ions scattered from a cell into a 360° cone of width $\Delta\theta$ at θ. The solid angle in this apparatus is therefore about 300 times larger than that of conventional methods, allowing us to observe low energy scattering at large laboratory

[1] T. O. Bush, "Large Angle Scattering of Lithium Ions by Helium Atoms," unpublished Ph.D. thesis, Naval Postgraduate School, Monterey, California, 1968.
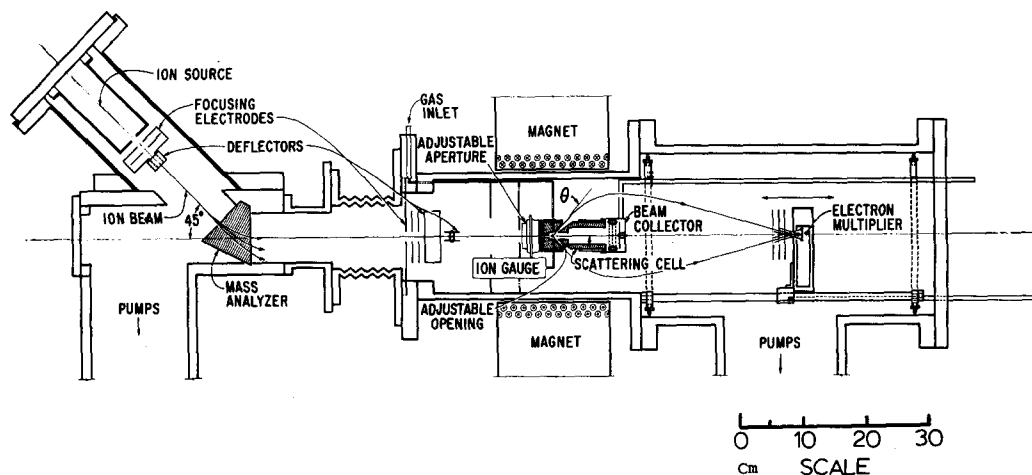
Fig. 1. Schematic of the experimental apparatus. The origin of the scattered ion trajectory is located at the center of the magnetic field. The electron multiplier is movable from outside the vacuum system.

angles. In addition, the scattered particles are automatically momentum analyzed by the magnetic field.

TRAJECTORY CALCULATIONS

Basic Ideas

The focusing properties of axially symmetric magnetic fields are commonly used in the analysis of β-ray spectra in nuclear physics.[2] The simplest geometry is the axially symmetric uniform field. The trajectory of a charged particel in this field is a helix and the particle will cross the field line on which it originated after one complete revolution. As shown in Fig. 2 the distance Z_0 at which the ion returns to the Z axis depends on the momentum p, the charge q, the angle θ, and the magnetic field $\mathbf{B}$. The relationship among these quantities is

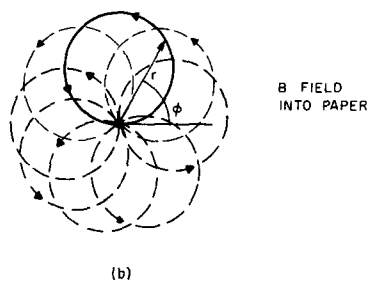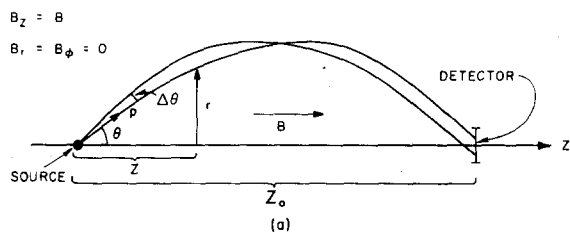$$Z_0 = 2\pi p \cos\theta / qB. \qquad (4)$$

(a)

(b)

Fig. 2. Orbit of a charged particle in a uniform magnetic field.

[2] K. Siegbahn, *Alpha-, Beta-, and Gamma-Ray Spectroscopy* (North Holland Publishing Co., Amsterdam, 1966).

Therefore a detector at Z_0 in a field B will "see" all ions of charge q scattered with a given momentum interval Δp at p into a conical shell $\Delta\theta$ at θ. There are two ways to scan different $(p/q)\cos\theta$ values: (1) Hold B constant and vary Z_0 by moving the detector; and (2) fix the detector at a particular value of Z_0 and then vary B. Since Eq. (4) is independent of the azimuthal angle ϕ, the entire 360° can in principle be observed.

In our particular apparatus the magnetic field is produced by a "thin" solenoid (Fig. 1) which produces a nonuniform axially symmetric magnetic field thus making numerical integrations necessary. This field geometry greatly increases the separation between adjacent trajectories thus enhancing the angular resolution for a fixed detector geometry (Fig. 3).

The well known technique of simulating the trajectory of a charged particle in a magnetic field using a current carrying flexible wire was employed to obtain preliminary data on the trajectories and to check our calculations.[3]

Magnetic Vector Potential

The trajectory equation for a charged particle in a *nonuniform* field is most conveniently expressed in terms of the magnetic vector potential $\mathbf{A}$. Therefore the measured field $\mathbf{B}$ of the focusing magnet must be expressed in terms of $\mathbf{A}$ before the orbits can be calculated.

For our geometry the current density $\mathbf{J}$ in the magnet is assumed to have only a ϕ component. Since

$$\mathbf{A} = \frac{\mu}{4\pi} \int \frac{\mathbf{J}(\mathbf{r})}{|\mathbf{r}|} dv, \qquad (5)$$

there is only a ϕ component of the magnetic vector potential. Busch[4] has shown for this case that $\mathbf{A}_\phi(r,z)$ can be ex-

[3] P. J. Kelly, "Analogue Measurements of Charged Particle Trajectories in an Inhomogeneous Magnetic Field," unpublished Master's thesis, Naval Postgraduate School, Monterey, California, 1965.
[4] H. Busch, Ann. Physik **81**, 974 (1926).

pressed as a function of the z component of the magnetic field on the symmetry axis, $B_z(r=0)$, namely,

$$A_\phi(r,z) = \sum_{n=0}^{\infty} \frac{(-1)^n}{n!(n+1)!}\left(\frac{r}{2}\right)^{2n+1}\frac{\partial^{2n}B_z(r=0)}{\partial z^{2n}}. \quad (6)$$

Therefore one needs to measure only $B_z(r=0,z)$ in order to calculate the magnetic vector potential. The measured values of $B_z(z)$ were fitted to a polynomial of the form

$$B_z(z) = \sum_{m=1}^{13} C_m z^{m-1}. \quad (7)$$

The field values obtained from this expression were within 0.1% of the experimentally measured values.

The equation of motion of the charged particles in the magnetic field is

$$\mathbf{F} = m\mathbf{a} = q(\mathbf{v}\times\mathbf{B}) = q\mathbf{v}\times(\nabla\times\mathbf{A}). \quad (8)$$

In cylindrical coordinates (r,ϕ,z) the force components are

$$F_r = m\left[\frac{d^2r}{dt^2} - r\left(\frac{d\phi}{dt}\right)^2\right] = q\left(\frac{d\phi}{dt}\right)\frac{\partial(rA_\phi)}{\partial r} \quad (9)$$

$$F_\phi = m\left[2\left(\frac{dr}{dt}\right)\left(\frac{d\phi}{dt}\right) + r\frac{d^2\phi}{dt^2}\right]$$
$$= -q\left[\left(\frac{dz}{dt}\right)\left(\frac{\partial A_\phi}{\partial z}\right) + \frac{1}{r}\left(\frac{dr}{dt}\right)\frac{\partial(rA_\phi)}{\partial r}\right] \quad (10)$$

$$F_z = m\frac{d^2z}{dt^2} = qr\left(\frac{d\phi}{dt}\right)\frac{\partial A_\phi}{\partial z}. \quad (11)$$

Using the two constants of motion, the total energy and the angular momentum, the time t and the variable ϕ can be eliminated to give

$$\frac{d^2r/dz^2}{[1+(dr/dz)^2]}[K^2 - A_\phi^2] - \frac{dr}{dz}\left[A_\phi\frac{\partial A_\phi}{\partial z}\right] + A_\phi\frac{\partial A_\phi}{\partial r} = 0, \quad (12)$$
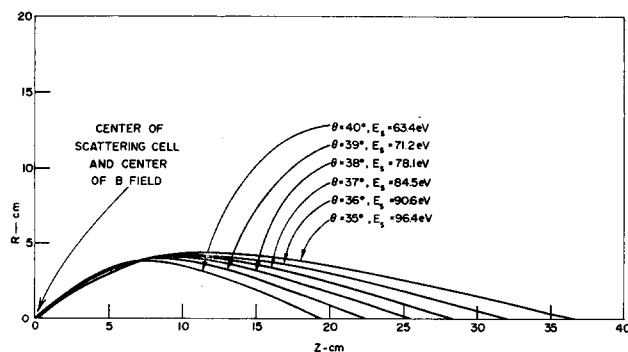

FIG. 3. Numerically computed ion trajectories for $^6Li^+$ on He at 200 eV. The magnetic field is the same for all trajectories, while the energy and angle are varied.

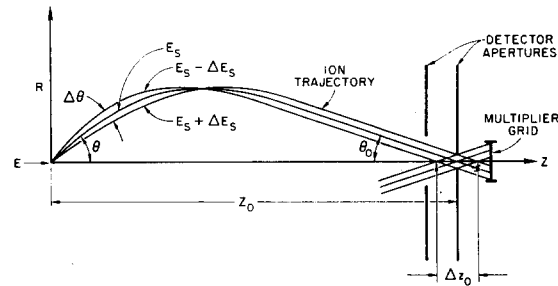FIG. 4. Angular and energy spread allowed by the detector aperture. Notice that Δz_0 is a measure of the "effective" detector aperture.

where $K^2 = p^2/q^2 = \text{const}$. Numerical integration of this equation for a given set of initial conditions (p,B,q,θ) yields $r = f(z)$. A typical set of computed trajectories is shown in Fig. 3. The difference between the computed trajectories and those obtained by the current carrying wire technique was less than 10% of the computed values at all points.

Angular Resolution

The major advantage of this experimental method is that all particles scattered into a conical shell $\Delta\theta$ at θ are collected. As seen in Figs. 1 and 4 a particle can enter the detector only if it crosses the axis within $Z_0 \pm \Delta Z_0/2$ and at the proper angle θ_0. The size of ΔZ_0 is a measure of both the angular resolution and the solid angle of the reaction being observed.

The angular spread $\Delta\theta$ depends on ΔZ_0 whose value in turn is determined by the detector geometry and the particular trajectory under observation. The relation between $\Delta\theta$ and ΔZ_0 can be found from the function relating the intercept distance Z_0 to the various trajectory parameters,

$$Z_0 = f(E,\theta,B,\rho,\eta,C), \quad (13)$$

where E is the energy of the incident ion, θ the angle of scatter, B the magnetic field equal to $f(I)$, I the coil current, ρ the target displacement from system axis along a radial line, η the target displacement from system center along the z axis, and C the constant for each reaction including mass ratios, inelastic energy losses, etc. Differentiating this gives

$$\Delta Z_0 = \left(\frac{\partial Z_0}{\partial E}\right)\Delta E + \left(\frac{\partial Z_0}{\partial \theta}\right)\Delta\theta + \left(\frac{\partial Z_0}{\partial B}\right)\Delta B$$
$$+ \left(\frac{\partial Z_0}{\partial \rho}\right)\Delta\rho + \left(\frac{\partial Z_0}{\partial \rho}\right)\Delta\eta + \left(\frac{\partial Z_0}{\partial C}\right)\Delta C. \quad (14)$$

However, for a specific reaction and measurement $\Delta B = 0$ and $\Delta C = 0$, and the above expression reduces to

$$\Delta Z_0 = \left(\frac{\partial Z_0}{\partial E}\right)\Delta E + \left(\frac{\partial Z_0}{\partial \theta}\right)\Delta\theta + \left(\frac{\partial Z_0}{\partial \rho}\right)\Delta\rho + \left(\frac{\partial Z_0}{\partial \eta}\right)\Delta\eta. \quad (15)$$
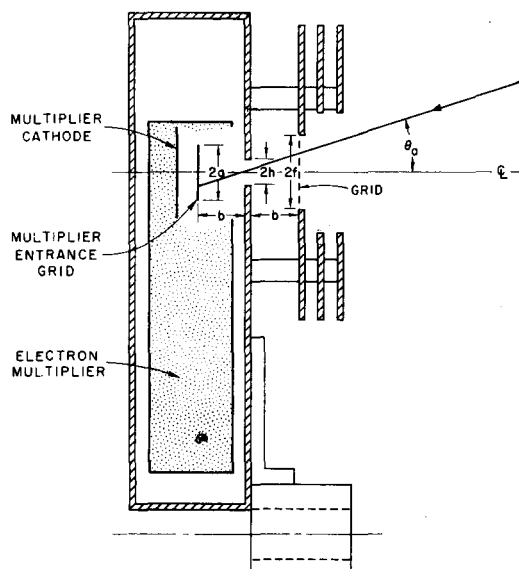
FIG. 5. Detector aperture geometry. a=0.71 cm, b=1.27 cm,
f=0.95 cm, h=0.32 cm.

Solving for the angular spread gives

$$\Delta\theta = \Delta Z_0 - \left(\frac{\partial Z_0}{\partial E}\right)_{\theta,\rho,\eta}\Delta E - \left(\frac{\partial Z_0}{\partial \rho}\right)_{E,\theta,\eta}\Delta\rho$$

$$- \left(\frac{\partial Z_0}{\partial \eta}\right)_{E,\theta,\eta}\Delta\eta \bigg/ \left(\frac{\partial Z_0}{\partial \theta}\right)_{E,\rho,\eta}. \quad (16)$$

Since there is no analytical expression for the various differentials they must be evaluated separately by solving a number of trajectories where E, θ, ρ, and η have been appropriately varied. The terms $\Delta\rho$ and $\Delta\eta$ are difficult to calculate exactly. However, we estimate that their effect is to change $\Delta\theta$ by no more than 10% and they have been neglected. In the Appendix we consider this correction in more detail for the special case of a uniform B field where precise calculations are relatively simple. The correction due to the energy spread in the incident ion beam is quite small for the Li$^+$ ion source (source $\Delta E < 0.25$ eV) and has also been neglected. Thus the angular spread for a particular reaction can be expressed as

$$\Delta\theta \approx (\partial\theta/\partial Z_0)_E \Delta Z_0. \quad (17)$$

The intercept spread ΔZ_0 depends on the detector aperture geometry and the intercept angle θ_0. Since any two of the three detector apertures (Fig. 5) can limit the size of an incoming beam of ions there are three expressions for ΔZ_0 derivable from our particular geometry

$$\Delta Z_0 = (f+a)\cot\theta_0 - 2b \quad \text{for} \quad 33.2° \geq \theta_0 \geq 26.6°, \quad (18)$$

$$\Delta Z_0 = (h+a)\cot\theta_0 - b \quad \text{for} \quad 26.6° \geq \theta_0 \geq 17.3°, \quad (19)$$

$$\Delta Z_0 = 2h\cot\theta_0 \quad \text{for} \quad 17.3° \geq \theta_0 \geq 0°, \quad (20)$$

where θ_0 is uniquely determined from the computed trajectories. Using the appropriate ΔZ_0 expression and Eq. (17) the angular resolution for the reaction ^{6}Li$^+$ on He at 300 eV, $I = 13.0$ A, $\Delta E = 0.25$ eV, and $\theta = 39.6°$ is found to be 0.38°, which is representative of the $\Delta\theta$ values observed in these measurements.

Energy Resolution

Another important quantity is the spread in energies, ΔE_s, that particles scattered at a particular θ may have and still be detected. This quantity depends upon $\Delta\theta$ at θ, the incident ion energy E, and the reaction parameter C. Therefore

$$E_s = E_s(E,\theta,C) \quad (21)$$

and

$$\Delta E_s = (\partial E_s/\partial E)_\theta \Delta E + (\partial E_s/\partial\theta)_E \Delta E. \quad (22)$$

For the ^{6}Li$^+$ on He reaction mentioned above with $\Delta E = 0.25$ eV we get $\Delta E_s = 3.8$ eV as a typical value for the energy resolution.

Solid Angle

The solid angle for scattering from any point (ρ,η) within the target volume is given by

$$d\Omega(\rho,\eta,\theta) = 2\pi \sin\theta\Delta\theta(\rho,\eta,\theta)\,(\text{sr}) \quad (23)$$

from which we can, in principle, obtain $d\Omega(\theta)$ by integration over the target volume. However in the absence of an analytic expression for $\Delta\theta(\rho,\eta,\theta)$ we approximate $\Delta\theta$ by noting that particles scattered at θ from $\rho=0$ and $\eta=0$ which cross the axis in ΔZ_0 at Z_0 (Fig. 4) will be counted. This ΔZ_0 determines the angular resolution $\Delta\theta$ which the detector sees and we have used this "central" $\Delta\theta$ to compute $d\Omega$ from

$$d\Omega = 2\pi \sin\theta\Delta\theta = 2\pi \sin\theta(\partial\theta/\partial Z_0)_E \Delta Z_0 \,(\text{sr}). \quad (24)$$
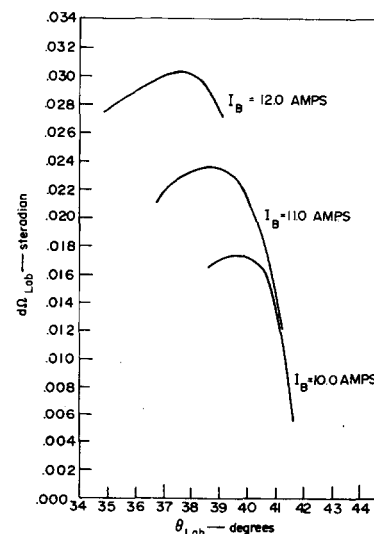

FIG. 6. Solid angle vs angle of scatter for the elastic scattering of ^{6}Li$^+$ on He at 200 eV incident ion energy.

This expression must be evaluated for every trajectory to be measured since it depends not only on the angle of scatter, θ, but also on ΔZ_0 and the derivative $(\partial\theta/\partial Z_0)_E$. Representative values of the solid angle are shown in Fig. 6 for the reaction $^6Li^+ + He$ at 200 eV incident ion beam energy.

Target Thickness

In order to calculate the cross sections from the experimental measurements one must know the thickness of the target a scattered ion sees. In our apparatus the target thickness t depends on the scattering cell exit slit geometry and the angle of scatter. The exit slit in the scattering cell has a forward edge which makes an angle of 49° with the system axis and rear edge which makes an angle of 36° with the system axis. The target thickness for ions scattered at angles from 36 to 49° is essentially the length S of the smallest opening in the exit slit. This distance can be set for any desired value from 0.0 to 0.8 cm. For ions scattered at less than 36° the target thickness is

$$t = S - 2.54 \sin(36° - \theta)/\sin\theta. \qquad (25)$$

For ions scattered at greater than 49° the target thickness is

$$t = S - 2.0 \sin(\theta - 49°)/\sin\theta. \qquad (26)$$

EXPERIMENTAL DETAILS

Ion Beam

The size and shape of the various components were largely determined by the physical dimensions of the focusing magnet and the strength of the magnetic field. The vacuum was maintained by two 15 cm diffusion pumps
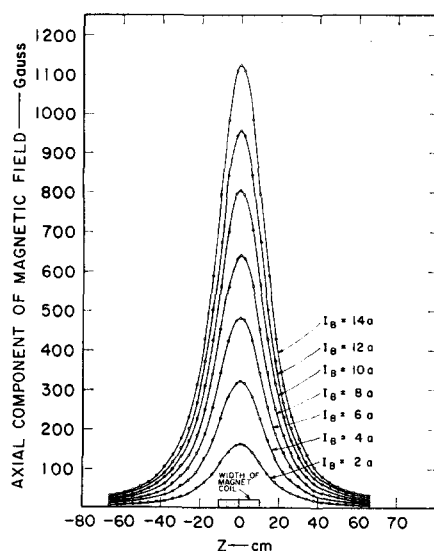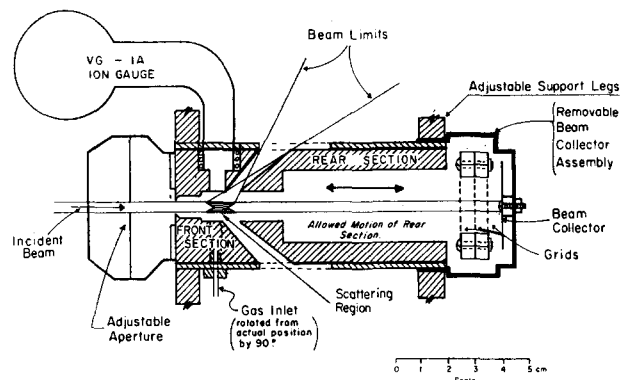
FIG. 8. Scattering cell and beam collector schematic cross section.

having water cooled baffles and liquid nitrogen cold traps. With gas in the scattering cell at a pressure 2.0×10^{-3} Torr the pumps maintain the detector chamber at 2.0×10^{-5} Torr and the mass analysis chamber at 4.0×10^{-6} Torr.

The lithium ion source used was essentially the source described by Heinz and Reeves.[5] It is a thermal emitter consisting of a very porous tungsten matrix into which the mineral beta-eucryptite $(Li_2O\cdot Al_2O_3\cdot 2SiO_2)$ has been fused. The lithium ions are produced when the tungsten matrix is heated to temperatures in excess of 1100°C. At about 1170°C the emitter delivered up to 1.0×10^{-7} A into the scattering cell. The energy spread in the ion beam was less than 0.25 eV in the energy range 15–800 eV.

A mass analyzer, designed and calibrated by Strohsahl,[6] was placed between the ion source and the scattering cell. The analyzer had a 45° angle of bend and a maximum field strength of up to 4000 G. This allowed up to 90% beam transmission and a mass resolution $(\Delta m/m)$ of about 40 for singly charged particles of mass number up to 40 and energies up to 1 keV.

One effect resulting from the use of the mass analyzer was the reduction of the background signal at the detector by a factor of 100 or more.

Focusing Magnet

The magnetic field in our experiments was produced by a coil consisting of five concentric brass spools wound with a total of 7938 turns of No. 15 wire. A Hall probe, calibrated in a uniform magnetic field against a known nuclear magnetic resonance probe accurate to ±1 G at 1000 G, was used to measure the field. The axial field component on the z axis was measured at 4 cm intervals from -66 cm to $+66$ cm for each of seven current settings. A plot of these measurements is shown in Fig. 7. Five contour plots of B as a function of r and ϕ were made in the planes defined by $Z=\pm42$ cm and 0 cm, to check the axial symmetry.

FIG. 7. Axial magnetic field strength at various distances and currents measured along the magnet axis.

[5] O. Heinz and R. T. Reeves, Rev. Sci Instrum. **39**, 1229 (1968).
[6] G. H. Strohsahl, "Construction and Calibration of a Mass Spectrometer for the Analysis of Light Ions," unpublished Master's thesis, Naval Postgraduate School, Monterey, California, 1967.

Scattering Cell

The stainless steel scattering cell is shown in Fig. 8. Physical obstacles such as support rods actually reduce the azimuthal collection angle from 360 to about 290° for our apparatus. Attached to the front of the scattering cell is a circular iris aperture of variable diameter which can be adjusted from outside the vacuum system thus permitting a check of the alignment of the system with the beam on. The ion currents to various sections of the scattering cell can be monitored independently. The rear section of the scattering cell can be moved horizontally from outside the vacuum system thereby adjusting the width of the slit through which the scattered particles leave from 0 to 0.8 cm.

The beam collector has three suppressor grids. Normally, the grid farthest from the collector was grounded, the middle grid was given a small positive potential to keep slow positive ions from reaching the collector, and the grid nearest the collector was given a small negative potential to suppress secondary electron emission from the collector. The collector was kept at ground potential. The beam collector and its grids are placed inside a metal shield which also acts as a gas cap over the rear end of the scattering cell. The beam collector assembly is mounted such that the assembly may be swung out of the path of the incident ion beam permitting alignment of the entire apparatus along the magnet axis and to allow the incident ion beam to fall directly on the detector for calibration purposes.

Scattered Ion Detector

A model 306 magnetic electron multiplier manufactured by Bendix Corporation, Cincinnati, Ohio was chosen as the beam detector and amplifier. This multiplier, developed
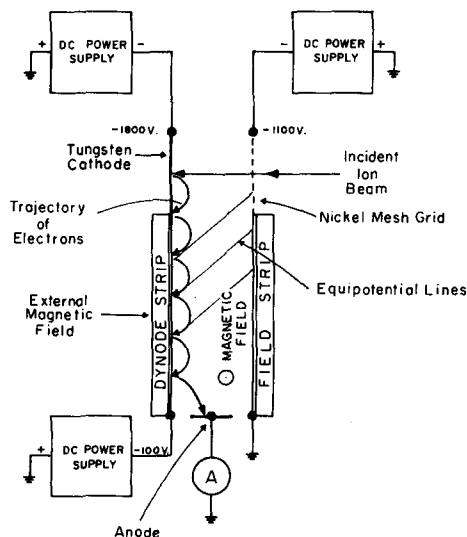
FIG. 9. Operational schematic of the Bendix model 306 magnetic electron multiplier which was used as the scattered ion detector.
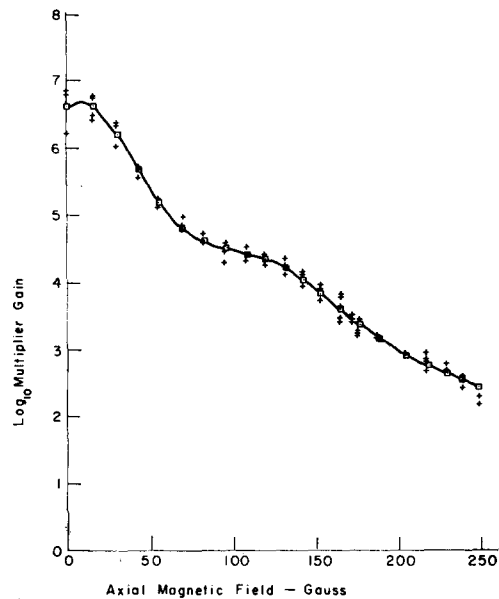
FIG. 10. $\log_{10}$ multiplier gain as a function of the axial magnetic field strength for a particular set of multiplier potentials. The solid line is a 10th order fit of the measured points. Multiplier settings: $V_{DSI} = -2100$ V, $V_{DSO} = -100$ V, $V_{FSI} = -1500$ V, $V_{FSO} = $ GND. +— measured values; ⊡—computed 10th order fit, standard deviation $=0.5$

by Goodrich and Wiley,[7] could provide reproducible current gains up to 10^6. A schematic view of the multiplier is shown in Fig. 9.

As the scattered ion detector in the experimental apparatus, the multiplier has to be operated in a magnetic field of up to 200 G. The effect of this magnetic field causes the secondary electrons of the multiplier to drift perpendicular to the long axis of the dynode strip. Thus some of these electrons drift off the side of the dynode strip and never reach the anode, thereby reducing the gain of the multiplier. The rate of drift increases with increase in the magnetic field, causing the multiplier gain to decrease with increasing field. Shielding the multiplier from the external field was attempted using Mu-metal, Netic, and Co-netic foils. This proved unsatisfactory for two reasons. First, the large amount of shielding material required so disturbed the focusing field that scattered particle trajectories were not predictable. Second, the gain of the multiplier could not be reproduced when the focusing field was changed and then returned to the original value. This was probably due to the hysteresis in the shielding material. The most satisfactory solution has been to operate the multiplier inside an aluminum shield to protect it from random background and to choose the various strip potentials which give the highest gain and lowest noise. For a particular set of potentials the multiplier gain was measured at different magnetic field values. This was done by varying the magnet coil current and keeping the multiplier at a fixed distance from the

[7] G. W. Goodrich and W. C. Wiley, Rev. Sci. Instrum. **32**, 846 (1961).

magnet center and also by fixing the coil current and varying the distance of the multiplier from the magnet center. Both methods gave essentially the same gain for equal values of the axial magnetic field. A plot of these measurements and a 10th order fit of the data points are shown in Fig. 10. The fitted value was used in the actual calculation of cross sections. An actual gain measurement is made as follows: The field strip and the anode of the multiplier are grounded while the cathode is connected to an ammeter and the ion beam from the source is directed onto the cathode. This current (which has to be kept below 10^{-11} A to prevent saturation of the multiplier output) is thus directly measured. Then, without changing the incident current on the multiplier cathode, the multiplier is placed in its normal operating condition and the anode current is again measured. The ratio of the amplified anode current to the direct ion beam current measured at the cathode is the gain. This process is then repeated for each new set of magnet currents and detector distances.

Measurements showed that the gain did not vary with gas pressure up to 2.0×10^{-4} Torr, a pressure much higher than the multiplier ever encountered when data were being taken. The gain was measured using ^{6}Li$^+$, ^{7}Li$^+$, ^{4}He$^+$, H$_2$$^+$, and H$^+$ and no mass dependence was detected. The gain was found to be independent of the anode current up to 10^{-5} A. Above these currents the multiplier tends to saturate since the anode current is approaching the strip current in magnitude. To prevent slow ions from entering the detector, a grid was placed over the detector shield aperture. Normally, a small positive potential (about 20 V) was sufficient to screen out this background. The grid also permits a crude analysis of the scattered ion energy.

After about two months' operation the multiplier strips became coated with vacuum pump oil. This caused large increases in the multiplier noise resulting in false current measurements. Cleaning the strips with a pencil eraser to remove the deposits reduced the noise but did not affect the multiplier gain.

System Alignment

Since the geometric center line of the focusing magnet coil was found to accurately coincide with the magnetic field axis the geometric axis was used as the reference for aligning all other components. The scattering cell, the detector, and the focusing lenses were easily aligned to the magnetic field axis to an accuracy of 1.0 mm. Analysis of computer trajectories showed this error to be undetectable.

The incident ion beam was aligned by adjusting the position of the source and the mass analyzer with the ion beam on until the maximum beam reached the scattering cell beam collector using no deflector voltages. Alignment was also checked by measuring the ratio of the current to the front of the scattering cell to the current on the beam collector with magnet on and magnet off.

EXPERIMENTAL RESULTS

Preliminary Tests

The differential scattering cross section shown in Eq. (3) can be rewritten in terms of the quantities actually measured as follows:

$$d\sigma(\theta) = [(I_D/G)/I_i(P_{sc}N_0)td\Omega] cm^2, \qquad (27)$$

where I_D is the current at MEM detector anode in amperes, G the MEM detector gain, I_i the incident ion beam current in amperes, P_{sc} the pressure of target gas in torricelli, $N_0 = 3.536 \times 10^{16}$ particles/cm$^3 \cdot$Torr, t is the target length in centimeters, and $d\Omega$ the solid angle in steradians.

In order to eliminate any spurious signals a series of measurements was undertaken to test the dependence of $d\sigma(\theta)$ on the variables I_i, P_{sc}, and t. For a particular angle of scatter and constant experimental conditions we note that

$$I_D = KI_iP_{sc}t \quad (K = \text{const}). \qquad (28)$$

Tests verified that the observed signal I_D was directly proportional to each of the parameters I_i, P_{sc}, and t. The results indicate that a scattered beam was indeed being measured.[1] For the differential scattering cross sections measured, the ion current at the beam collector was about 10^{-7} A, the current to the rear section of the scattering cell was about 10^{-9} A, the ion current on the front face of the scattering cell was about 10^{-8}, and the detector signal of the MEM output varied from 10^{-8} to 10^{-13} A. With no target gas in the scattering cell and essentially the same current to the beam collector the detector current drops to about 10^{-15} A. Consequently the signal due to scattered ions was at least 100 times greater than the multiplier dark current.
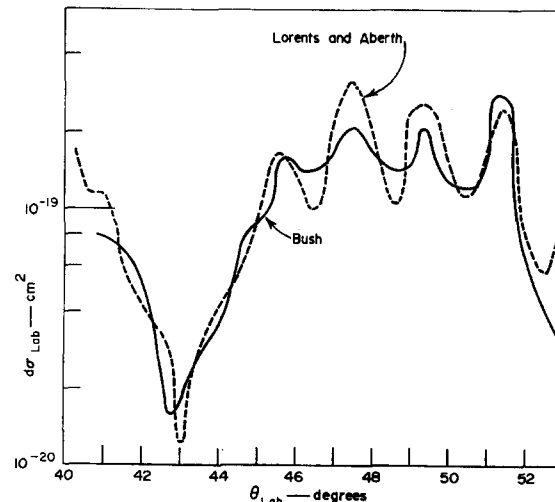

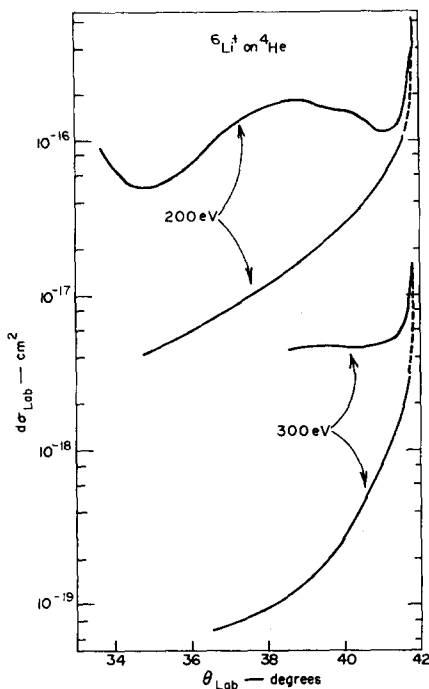FIG. 11. $d\sigma(\theta)$ vs θ for He$^+$ on He at 300 eV in the laboratory coordinate system.

FIG. 12. $d\sigma(\theta)$ vs θ for ^{6}Li$^+$ on He at 200 and 300 eV in the laboratory coordinate system.

He$^+$ on He Scattering Data

As another preliminary test of our technique, we made a measurement of the elastic differential scattering cross sections for He$^+$ on He at 300 eV from 40 to 52°, and compared our data with the more precise measurements of Lorents and Aberth.[8] The results are shown in Fig. 11. It can be seen that the agreement is quite good. It should be pointed out however that the angular resolution is a critical function of the energy spread in the incident beam and that any misalignment, which leads to spiraling of the incident particles, will also lead to loss of angular resolution.

^{6}Li$^+$ on He Scattering Data

Finally, a measurement on the elastic differential scattering cross sections of ^{6}Li$^+$ on He was carried out. Since, for this system, the helium target atoms have a smaller mass than the incident lithium ions there are two possible energies at which the lithium ion may scatter at any allowable laboratory scattering angle. There also is a maximum angle of scatter in the laboratory system determined by the relation

$$\theta_{max} = \sin(M_{He}/M_{Li}) = 41.7°. \qquad (29)$$

At this maximum scattering angle the laboratory elastic cross section becomes infinite. This particular property made this system suitable for a check of the accuracy of our angular determination and system alignment. Since our experimental apparatus does not detect particles

[8] D. C. Lorents and W. Aberth, Phys. Rev. **139**, A1017 (1965).

scattered at a particular angle, but rather at a particular vector momentum, this peak in the laboratory cross section can be seen by setting the detector at a convenient distance from the scattering center and slowly decreasing the magnet current. This allows us to measure the cross sections continuously from the high energy side to the low energy side of θ_{max} without moving the detector out of the scattered particle beam and thereby obtain an absolute calibration of the computed trajectories. The results of these measurements are shown in Fig. 12 which are plots of the laboratory differential scattering cross section vs the angle of scatter at 200 and 300 eV. Notice that in both cases the upper branch, corresponding to high scattering energies, suddenly increases sharply as we approach $\theta_{max}(41.7°)$ and then decreases along the lower branch as the angle of scatter decreases. The fact that the cross section peak appears at the correct angle illustrates that our angular determination is correct and our system is properly aligned. The total spread in the data is about a factor of 2 and is believed to be largely due to variations in the multiplication factor of the magnetic electron multiplier from run to run. The same data are shown in the center of mass systems in Fig. 13. There appears to be some structure in both curves. However, from these data, it is not possible to conclude whether this structure is due to instrumental effects or represents an oscillation in the cross section produced by quantum mechanical interference effects. For comparison purposes an extrapolation of the data of Lorents and Aberth[9] is also shown in Fig. 13. The extrapolation used the potential due to Berry and Zehr[10] which is given by $V(r) = 13.6 \exp(-2.7R)$ a.u. However, several other potentials which can be used all yield approximately the same extrapolated curve.
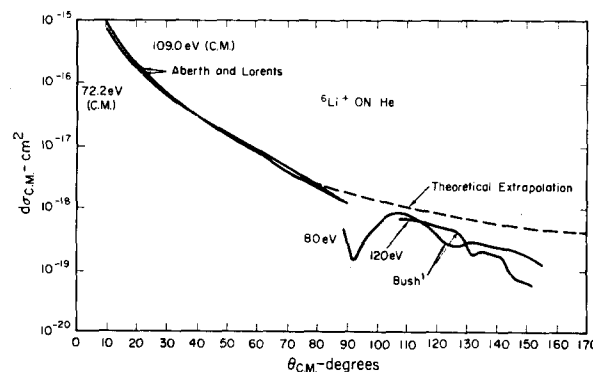

FIG. 13. Elastic differential scattering cross section for ^{6}Li$^+$ on He at 80 and 120 eV in the center of mass coordinate system. The extrapolated cross sections from Lorents and Aberth[9] are also shown.

[9] W. Aberth and D. C. Lorents, *4th International Conference on the Physics of Electronic and Atomic Collisions* (Science Bookcrafters, Inc. Hastings-on-the-Hudson, N. Y., 1965), p. 269; private communication.

[10] F. J. Zehr and H. W. Berry, Phys. Rev. **159**, 13 (1967).

Experimental Errors

There are several sources of error in the measurements. One source of error which cannot be entirely eliminated arises from the spiraling of the incident ions about the focusing magnet axis. As already pointed out above this introduces an error in the angular measurement and is most important in measurements where the cross section has rapid variations as a function of the scattering angle. However, the effect is minimized by proper alignment of the incident beam to the focusing magnet axis. The gain of the MEM, which is the scattered ion detector, is a rather sensitive function of the magnetic field strength. Thus any small error in setting the magnet current or the detector distance would result in actual gains slightly different from those used in the cross section calculations. The error in setting the detector distance and the magnet current would also cause differences between the actually observed angle of scatter and solid angle and their expected values from which the cross sections are calculated. The detector distance can be set to ± 1 mm and the magnet current can be regulated to ± 0.05 A. For the ^{6}Li$^+$ on He data this results in a possible error in the scattered angle of less than 0.05° and in the solid angle of less than 5%. Another source of error is in the measurement of the target gas pressure in the scattering cell. Although an accurate determination of this error was not possible it is apparent from the scattering cell geometry that the actual pressure is higher than the measured pressure used in the cross section calculation. It is felt that the primary source of scatter in our data is due to the multiplier noise caused by surface contamination. An analysis of the cross sections for ^{6}Li$^+$ on He gives a precision which is on the order of $\pm 20\%$ of the average value of each set of measurements.

ACKNOWLEDGMENTS

APPENDIX: SOLID ANGLE AND SOURCE VOLUME FOR THE UNIFORM FIELD CASE

Equations (3) and (27) show that under specific conditions the differential scattering cross section is inversely proportional to the average values of the target thickness, and the solid angle subtended by the detector. Calculations are underway to determine these quantities more accurately than the averages used in the text. The special case of a uniform B field where analytic solutions for the tra-
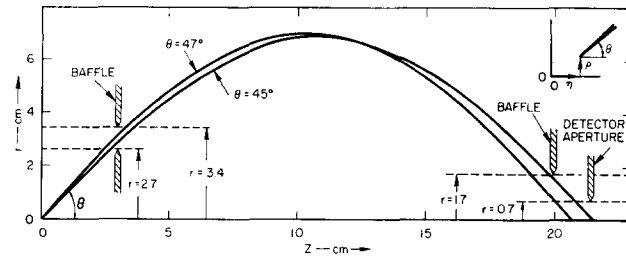

FIG. A1. Geometry of the uniform B field spectrometer. Trajectories shown are for elastic scattering of 100 eV ^{6}Li$^+$ by Ne with $B = 662$ G.

jectories are possible is worked out here to demonstrate the methods employed in the general case.

Assume the beam to be incident in a uniform B field parallel to the z axis of a cylindrical coordinate system with its origin near the center of the source volume. Assume further that the incident beam is uniform, parallel, and monoenergetic, has a radius ρ_{max}, and has its center line along the z axis. If the attenuation of the beam in the source volume is negligible, then the effective source thickness t can be shown to be the source volume divided by the maximum cross sectional area $\pi \rho_{max}^2$, and the effective solid angle $d\Omega(\bar{\theta})$ is the volume weighted average of the solid angle over the source volume.

Consider a scattering event with scattering angle θ originating at a point $r = \rho$, $z = \eta$ near the origin (see Fig. A1). The projection of the initial position vector on a plane perpendicular to the z axis makes an angle ν with the projection of the initial momentum vector of the scattered particle. The trajectory corresponding to given values of θ and ν has the following set of initial conditions:

$$r = \rho, \quad z = \eta \quad \text{and} \quad dr/dz = \tan\theta \cos\nu.$$

Integration of the equation of motion with these initial conditions (and a given value of the magnitude of the initial momentum) yields the trajectory

$$r^2 = \rho^2 + r_m^2 \sin^2\gamma + 2\rho r_m |\sin\gamma| \cos(\gamma + \nu),$$

where $r_m = 2p \sin\theta / qB$, $\gamma = (z - \eta/r_m) \tan\theta$, B is the magnetic induction, and q and p are the charge and initial momentum of the scattered particle.

Consider some point ρ, η within the source volume. The solid angle which the detector subtends at this point is determined by the ranges of θ and ν for which particles will reach the detector. The shaded area in Fig. A2 indicates these ranges for a typical point ($\rho = 0.15$ cm, $\eta = 0.3$ cm). The data shown were obtained by solving the equation of motion for suitable values of θ and ν and determining whether or not the resulting trajectories will clear a set of fixed baffles (see Fig. A1).

ν was divided into 10° intervals and θ into 0.2° intervals. Thus the boundary of the above "area" is uncertain to within these limits. The solid angle at the point ρ, η is ob-

t ained directly from this plot since

$$\Omega(\rho,\eta)=\int_{\theta_i(\rho,\eta)}^{\theta_f(\rho,\eta)}\int_{\nu_i(\rho,\eta,\theta)}^{\nu_f(\rho,\eta,\theta)}\sin\theta\,d\nu\,d\theta. \quad (A1)$$

The extent of the source volume can be determined by repeating this process for a grid of ρ and η values. We chose the intervals as 0.05 cm for ρ and 0.10 cm for η, and all points of the grid for which $\Omega(\rho,\eta)$ is positive thus lie within the source volume; those points for which $\Omega(\rho,\eta)$ is zero lie outside the source volume. Thus, a systematic calculation over the entire grid network establishes the extent of the source volume and determines values of the function $\Omega(\rho,\eta)$ at representative points within the source volume. Figure A3 displays the solid angle function $\Omega(\rho,\eta)$ over the range of η for three different ρ values. Extrapolation of the axial ends of these curves gives a good estimate of the axial extent of the source volume. This feature is also illustrated on Fig. A3 which shows the extent of the source volume in ρ, η space.

The function $\Omega(\rho,\eta)$, known over the extent of the source volume, can now be used to evaluate the effective solid angle $d\Omega(\bar{\theta})$. This can be shown to be the volume averaged value of the solid angle distribution, i.e.,

$$d\Omega(\bar{\theta})=\frac{1}{V}\int_0^{\rho_{\max}}\int_{\eta_i(\rho)}^{\eta_f(\rho)}2\pi\rho\Omega(\rho,\eta)d\eta\,d\rho, \quad (A2)$$

where

$$V=\int_0^{\rho_{\max}}\int_{\eta_i(\rho)}^{\rho_f(\rho)}2\pi\rho\,d\eta\,d\rho.$$

Consider an element of source volume $2\pi\rho\,d\rho\,d\eta$ at the point ρ, η. The total number of detectable scattered particles originating from this volume element is proportional to the product $\Omega(\rho,\eta)\ 2\pi\rho\,d\rho\,d\eta$ and the total number of detectable particles is proportional to the volume integral of this expression which is seen to be $Vd\Omega(\bar{\theta})$.
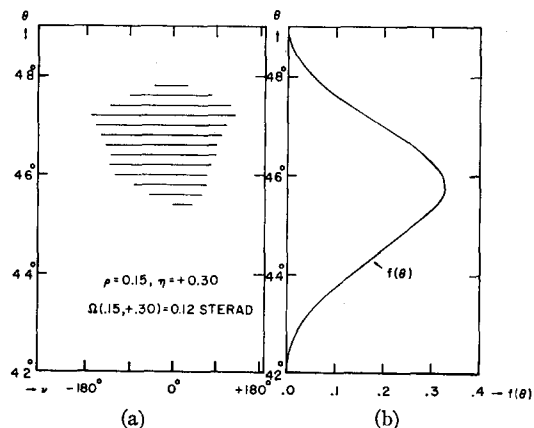

FIG. A2. (a) Detectable θ, ν values for a typical source volume point and (b) distribution function $f(\theta)$ of the scattering angle as a function of θ.
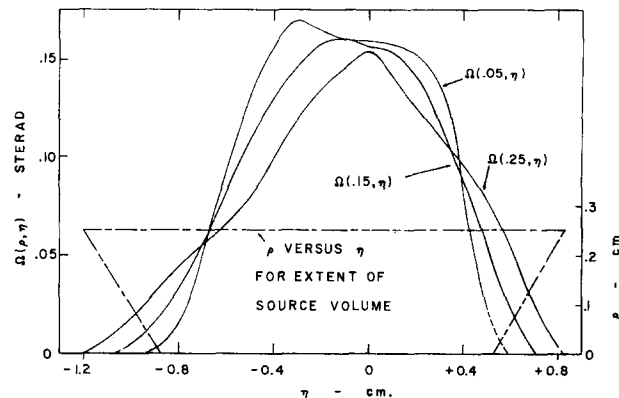

FIG. A3. Geometry of the source volume, and the solid angle distribution over the source volume.

It can be shown that the source volume integral of the expression

$$\left[2\pi\rho\,d\eta\,d\rho\int_{\gamma_i(\rho,\eta,\theta)}^{\gamma_f(\rho,\eta,\theta)}d\gamma\,\sin\theta\right]d\theta \quad (A3)$$

is proportional to the number of detectable scattered particles originating between θ and $\theta+d\theta$, and that the ratio of the above volume integral (without the $d\theta$ factor) to $Vd\Omega(\bar{\theta})$ is equal to $f(\theta)$, the normalized distribution function for the scattering angle θ. This function has been calculated for the example with results shown in Fig. A2 and is used to give the mean scattering angle,

$$\bar{\theta}=\int_{\theta_{\min}}^{\theta_{\max}}\theta f(\theta)d\theta$$

and the root mean square deviation of the scattering angle,

$$\Delta\theta_{\mathrm{rms}}=\left[\int_{\theta_{\min}}^{\theta_{\max}}(\theta-\bar{\theta})^2f(\theta)d\theta\right]^{\frac{1}{2}},$$

where $\theta_{\min}$ and $\theta_{\max}$ represent the extreme values for the scattering angles of detectable particles. For the numerical example, $\bar{\theta}=45.68°$ and $\Delta\theta_{\mathrm{rms}}=1.18°$; approximately 67% of the scattered particles lie within the range $45.68°\pm1.18°$. Note that $f(\theta)$ is somewhat asymmetrical about the value of θ at the peak.

In Table I the numerical values of the mean scattering

TABLE I. Comparison of calculated scattering angle, etc., with approximate values.

	Detailed calculations	Usual approximations
Mean scattering angle	45.68°±1.18°	46.0°±1.0°
Source thickness	1.85 cm	1.0 cm
Solid angle	0.0873 sr	0.16 sr
(Source thickness) ×(solid angle)	0.162 cm·sr	0.16 cm·sr

angle with its deviation, source thickness, solid angle, and product of source thickness and solid angle are listed. The values in the first column were obtained from the foregoing analysis. The values in the second column were obtained using the approximations applied in the nonuniform field case (see main section of paper).

By referring to Fig. A1 we see that for trajectories starting at the origin, the two extreme scattering angles are 45 and 47° with 46° being the geometrical mean, 0.3° larger than the actual value. The above angular spread corresponds to a solid angle of 0.16 sr subtended for a point at the origin. If the detectable scattering angle spread is determined vs η for points on the axis of symmetry, it is found that the "thickness" at half-maximum is approximately 1.0 cm. Thus the usual approximations underestimate the source thickness and overestimate the solid angle, but their product is in good agreement with the more precise value.

The reasons for this may be seen qualitatively by referring to Fig. A3. The $\Omega(\rho,\eta)$ vs η curves roughly correspond to trapezoids whose maximum heights are 0.16 sr and whose widths at half-maximum are approximately 1.0 cm. If for each value of ρ we represent these trapezoids by rectangles of width 1.0 cm and height 0.16 sr, then the source volume average value of solid angle is simply $0.16 \times 1.0/1.9 = 0.084$ sr which happens to agree very well with the accurate value, and thus indicates why the two different products of solid angle and thickness agree. Since this agreement may well be fortuitous for this special case we plan to extend our analysis to the nonuniform field case

Spectroscopic Method for Simultaneous Determination of Species Concentration and Temperature in a Cyclic Combustion Process*

D. S. SMITH AND E. S. STARKMAN

Department of Mechanical Engineering, University of California, Berkeley, California 94720

(Received 14 July 1969; and in final form, 21 August 1969)

An optical method for the simultaneous determination of species concentration and temperature in a high pressure transient combustion and expansion process is described. The experimental system utilizes a mechanically chopped (2000 Hz) external radiation signal to perturb the self-emission signal from the combustion gas of an internal combustion engine. Distinguishing between the emission and absorption signals simultaneously provides a capability for determination of species concentration by absorption and of optical temperature by an emission–absorption technique.

INTRODUCTION

THE usual method for determining combustion gas composition is by physical sampling techniques, followed by continuous or batch analysis. Chemical, optical, and mass spectrometric methods have all been successfully employed in measuring concentrations of stable species in low and high pressure combustion processes for both steady state and transient conditions.[1,2] Where the species are highly reactive, measurement must be made by optical or mass spectrometer and usually the work has been restricted to low and intermediate pressure and to steady flow combustion systems. Optical methods have also been applied fairly extensively to temperature determination in steady and transient combustion systems.

The method described herein differs from prior investigations in the simultaneous and continuous optical determination of species concentration and of temperature of a highly transient species. Hydroxyl free radical (OH) was observed in this manner, at pressures up to 60 atm and expansions on the order of 10 atm/msec.

Analysis of internal combustion engine processes provided motivation for development of the method. Particularly, it was desired to investigate the influence of hydroxyl radical on conversion of carbon monoxide to carbon dioxide. (It is generally accepted that the mechanism $CO + OH \rightarrow CO_2 + H$ is responsible for the slow conversion of CO to CO_2 in a high temperature hydrocarbon/air combustion process.) It is also well known that the concentration of carbon monoxide in the exhaust exceeds chemical equilibrium. Thus it was desired to obtain continuous values of post-combustion gas temperature and of species concentration during the expansion process in the engine.

Direct cylinder sampling and mass spectrometry were considered for the determination of species concentration. For such method, rapid conversion of the gas stream to a molecular beam would be required. Particularly, rapid

[1] R. M. Fristrom and A. A. Westenberg, *Flame Structure* (McGraw-Hill Book Company, New York, 1965).

[2] H. K. Newhall and E. S. Starkman, Trans. Soc. Automotive Eng. **76**, 743 (1968).